ARTICLE

Biocompatible photosensitizer with high intersystem crossing efficiency for precise two-photon photodynamic therapy

zReceived 00th January 20xx,
Accepted 00th January 20xx

DOI: 10.1039/x0xx00000x

Zhourui Xu, [a] Yihang Jiang, [a] Yuanyuan Shen, [a] Lele Tang, [b] Zulu Hu, [a] Guimiao Lin, [c] Wing-cheung Law, [d] Mingze Ma, [a] Biqin Dong, [e] Ken-Tye Yong, [f,g] Gaixia Xu, [a] Ye Tao, [*b] Runfeng Chen, [*b] and Chengbin Yang[*a]

Photodynamic efficiency is strongly dependent on the generation rate of reactive oxygen species (ROS) and the tissue penetration depth. Recent advances in materials science reveal that organic molecules with room-temperature phosphorescence (RTP) can potentially serve as efficient photosensitizers, owing to the limited dark cytotoxicity and abundant triplet excitons upon light irradiation. In this study, we combine RTP material with the two-photon excitation technique to both improve the ROS generation, therapeutic precision, and tissue penetration of photodynamic therapy. We succesfully prepared a novel RTP-based photosensitizer (BF_2DCz) with a high photoluminescence quantum yield of 47.7 ± 3% and remarkable intersystem crossing efficiency of ~90.3%. By encapsulation into the bovine serum albumin (BSA) matrix, BF_2DCz-BSA exhibits excellent biocompatibility, negligible dark toxicity, and superior photostability. Excitation with the femtosecond laser causes BF2DCz-BSA to efficiently generate ROS and precisely exert cell damage at the desired location.

Introduction

Photodynamic therapy (PDT), as a novel tumor-ablative and function-sparing oncologic intervention, has attracted significant attention in clinical and research studies. [1] To date, nine phototherapeutic drugs have been approved for clinical use. [2] PDT involves the systematic administration of photosensitizers (PS) followed by illumination at the pathological site with a specific wavelength of light. [3] The excited PS either undergoes a radiative decay to the ground state via fluorescence emission (a property that can be used for bioimaging) or enriches the triplet excitons through intersystem crossing (ISC) followed by the generation of reactive oxygen species (ROS). [4] These ROS can induce cell death by oxidizing the intracellular biomacromolecules, including lipids, amino-acids, and proteins, leading to irreversible damage to vital subcellular targets such as the membrane and organelles. [5] Further, the limited lifetime (half-life: 0.03 – 0.18 ms) of ROS considerably restricts its diffusion in biological systems (within a radius of 0.02 μm), contributing to minimal collateral damage. [3] Hence, by considering its non-invasiveness, limited side effects, and specific spatiotemporal selectivity, PDT exhibits excellent anti-cancer effects and is considered as a better alternative to conventional standard therapeutic approaches in certain scenarios. [6-8]

Inspired by the promise held by PDT, the development of PS has attracted growing interest. [9] An ideal PS has negligible dark-toxicity, high ISC, an appropriate triplet lifetime, and deep penetration with long excitation wavelength. Over the past few decades, great progress has been made in exploiting suitable PS for clinical PDT. [10, 11] However, key limitations remain, including 1) moderate ROS production, and 2) low depth of tissue penetration, which severely inhibits their widespread use and limits the full potential of PDT. [2] Recent efforts in improving ROS production have been proposed by integrating heavy metal ions into the conjugated molecular structure. [12-14] The existence of heavy metal ions helps break the spin-forbidden transition between singlet and triplet states for improved ISC efficiency. [15] Despite the distinct PDT effect, biosafety issues owing to the potential leakage of heavy metal ions in living bodies pose an important risk for in vivo applications. Other efforts have been made to extend the optical working region of PS into the near infrared (NIR) range by prolonging the conjugation length between the electron donor and acceptor [16] or applying up-conversion nanoparticles as light transducers. [17] However, the redshifted light source [18] with limited up-conversion efficiency [19] may not be able to excite PS for sufficient ROS production.

[a.] *Guangdong Key Laboratory for Biomedical Measurements and Ultrasound Imaging, School of Biomedical Engineering, Health Science Center, Shenzhen University, 1066th Xueyuan Rd, Nanshan district, Shenzhen, Guangdong Province, China.*
[b.] *State Key Laboratory of Organic Electronics and Information Displays & Institute of Advanced Materials (IAM), Nanjing University of Posts & Telecommunications, 9th Wenyuan Road, Nanjing 210023, China.*
[c.] *Base for International Science and Technology Cooperation: Carson Cancer Stem Cell Vaccines R&D Center, Shenzhen Key Lab of Synthetic Biology, Department of Physiology, School of Basic Medical Sciences, Shenzhen University, 1066th Xueyuan Rd, Nanshan District, Shenzhen, Guangdong Province, China.*
[d.] *Department of Industrial and Systems Engineering, The Hong Kong Polytechnic University, 11th YukChoi Rd, Hong Hum, Kowloon, Hong Kong.*
[e.] *Guangdong Provincial Key Laboratory of Durability for Marine Civil Engineering, College of Civil and Transportation Engineering, Shenzhen University, 3688th Nanhai Rd, Nanshan District, Shenzhen, Guangdong Province, China.*
[f.] *School of Biomedical Engineering, The University of Sydney, Sydney, New South Wales 2006, Australia.*
[g.] *The University of Sydney Nano Institute, The University of Sydney, Sydney, New South Wales 2006, Australia.*

Electronic Supplementary Information (ESI) available: [details of any supplementary information available should be included here]. See DOI: 10.1039/x0xx00000x

In recent years, metal-free organic probes with room temperature phosphorescence (RTP) characteristics [20] have emerged as a new generation of materials that not only have robust triplet excitons, [21] but also circumvent the toxicity issue typically occurring in inorganic [22] or "heavy-metal-ions-containing" counterparts. [23, 24] Previous studies by our group revealed that RTP materials undergo a thermally activated afterglow emission (TAA) with highly boosted triplet electrons and exhibited a prolonged lifetime. [25] Considering the limited toxicity, high ISC, and long triplet lifetime, designing and preparing an ideal PS based on efficient RTP molecules is an elegant solution. Nevertheless, most reported RTP molecules, only excitable by ultraviolet or visible light, [26] are not biologically compatible. [27, 28] Two-photon excitation (TPE) is a feasible strategy to excite RTP molecules in the NIR range, wherein two NIR photons are absorbed simultaneously to realize the same effects excited by the single photon with half wavelength. [29] As an additional benefit, compared to single photon excitation, the material is only activated in a confined volume [18] due to the high requirement of photon density and the square dependence on the laser intensity. [30] However, to the best of our knowledge, TPE-PDT based on organic RTP materials have seldom been reported.

Herein, a newly engineered PS (BF_2DCz) with RTP features was designed and synthesized for fluorescence imaging-guided photodynamic therapy. The direct connection of carbazole and difluoroboron β-diketonate in BF_2DCz contributed to a strong intramolecular charge transfer (ICT) with a small singlet-triplet splitting energy (ΔE_{ST}) and an efficient ISC process. Meanwhile, the twisted donor-acceptor-donor (D-A-D) architecture efficiently disturbs the π–π stacking of carbazole units, giving rise to the aggregation-induced emission feature. Supported by the designing concept of TAA, the BF_2DCz nanoparticle exhibits an exceptional photoluminescence quantum yield (PLQY) of 47.7 ± 3% and remarkable ISC efficiency of ~90.3%. By encapsulation into the BSA matrix, BF_2DCz-BSA exhibits excellent biocompatibility and remarkable colloidal stability in the physiological environment. Excitation with the 800 nm femtosecond laser achieves precise and efficient cancer cell ablation at both horizontal and vertical levels of the cell samples. Furthermore, the deep tissue penetration of BF_2DCz-BSA was verified by brain vascular imaging and a selective blood-vessel closure, demonstrating the great potential of our design of novel PS for PDT by combining the two-photon excitable feature with RTP.

Results and discussion

The metal-free organic material of difluoroboron 1,3-di(9H-carbazol-9-yl) propane-1,2-dione (BF_2DCz) was synthesized by an efficient two-step reaction. Detailed syntheses and characterizations are described in the Experimental Section (*Experimental Section*, Figure S1-3). To endow BF_2DCz with good biocompatibility and dispersity, BF_2DCz-BSA was fabricated *via* the nanoprecipitation method by encapsulating hydrophobic BF_2DCz molecules into the bovine albumin (BSA) matrix (the encapsulation process is schematically illustrated in Figure 1a). The morphology and size of the as-prepared BF_2DCz-BSA was visualized by transmission electron microscopy (TEM), showing good dispersity of BF_2DCz-BSA (Figure 1b). The shape and diameter of BF_2DCz-BSA were examined by HR-TEM. The image indicates that BF_2DCz-BSA has a spherical shape with diameter of ~59 nm (Figure 1c). The STEM-EDX mapping shows an enriched distribution of boron (B) and fluorine (F) elements in the nanoparticle core, confirming the successful encapsulation of BF_2DCz (Figure 1d). The hydrodynamic size of BF_2DCz-BSA in PBS buffer was determined by dynamic light scattering (DLS). The size of BF_2DCz-BSA is mostly below 100 nm, and the mean diameter is calculated to be 68 ± 15 nm (Figure 1e), which is slightly bigger than the TEM size owing to the hydrated state of NPs. The structural stability of BF_2DCz-BSA was evaluated by DLS after prolonged storage time. The hydrodynamic size and the polydispersity index remain steady after 57 days in PBS buffer (pH=7.4) (Figure 1f), suggesting good colloidal stability of BF_2DCz-BSA. To further investigate the photostability and structural stability in physiological environment, BF_2DCz-BSA was dispersed in four different solutions, including PBS, DMEM, FBS, and DMEM+10% FBS. After 72 hours of co-incubation, no significant photoluminescence quenching, or agglomeration were observed. All samples exhibit their original colour under daylight, and simultaneously emit bright green emission under 365 nm light (Figure S4). The hydrodynamic size of BF_2DCz-BSA in PBS and cell culture media (DMEM+10%FBS) at pH=7.4 and pH=5 was further measured. As shown in Figure S5, the size of BF_2DCz-BSA remained stable in 14 days. These results clearly indicate the promising potential of BF_2DCz-BSA in bio-applications.

The steady-state photophysical properties of BF_2DCz in single molecular and nano-aggregated states were investigated using the ultraviolet-visible (UV-vis) spectrometer and photoluminescence (PL) spectrofluorometer. Evident absorption bands at ~380 nm (Figure S6a), attributed to the strong intramolecular charge transfer (ICT) in donor-acceptor-donor molecular skeleton, are found in both toluene and the nanoparticles (NPs) (Figure S7). The ICT effect was further confirmed by the solvent dependent PL emission, showing red-shifted spectra with the increase of solvent polarities ranging from toluene to chloroform (Figure S6b). Remarkably, BF_2DCz NPs in water exhibited significantly enhanced PL intensity compared to that (molecular state) in toluene, showing a photoluminescence quantum yield (PLQY) elevation from 6.3% to 47.7 ± 3%. This prominently enhanced PL emission is attributed to the suppressed molecular motion and vibration-induced non-radiative transition, [31] thus resulting in aggregation-induced emission in the nano-aggregated state. The AIE feature of BF_2DCz was further confirmed by the photoluminescence measurement of molecules in toluene/water solvent system (Figure S8). More importantly, besides the UV light excited PL emission, BF_2DCz NPs also can be readily stimulated by an 800 nm ultrafast NIR laser, rendering almost identical PL spectra to that of UV light excitation with a main emission peak at ~497 nm (Figure 1g). This demonstrates its capability of multi-photon excitation, which can be attributed to the combined strong aggregation state and efficient ICT effect. The fluorescent PL lifetimes of BF_2DCz in single molecular and nano-aggregated states were 6.30 and 2.7 ns for the main emission bands at ~510 and 497 nm (Figure S9), respectively. Furthermore, BF_2DCz NPs also exhibit a shoulder emission band at ~523 nm with a lifetime of 32 ms (Figure 1h), indicating the RTP character that was verified by the

phosphorescence spectrum and oxygen-sensitive emission (Figure S10). To obtain a deeper insight into the triplet involved PL process, the excited state properties of BF_2DCz NPs were investigated by femtosecond transient absorption (fs-TA) spectroscopy. As shown in Figure 1(i-j) and Figure S11a, the excited-state absorption (ESA) around ~580 nm becomes saturated at 0.2 ps and then quickly decays with the lifetime of 0.28 ps, exhibiting its singlet ESA feature at 580 nm. Notably, the ESA at 750 nm increases when the ESA at ~580 nm starts to decrease, and the dynamic trace at 750 nm yields three decay components of 4.18, 116.57, and 4398.6 ps (Figure 1j and Figure S11b), indicating that the peak around 750 nm must be assigned to triplet ESA. These results suggest the occurrence of intersystem crossing (ISC) for the population of the triplet state, and a fast ISC lifetime of 0.31 ps was fitted according to the dynamic rise trace at 750 nm, corresponding to the ISC rate of 3.2×10^{12} s^{-1}. This rapid ISC is attributed to the small singlet-splitting energy level of 0.13 eV as revealed by steady-state photoluminescence (SSPL, 497 nm) and phosphorescence (523 nm) spectra (Figure 1g, top). Using the decay rate of singlet ESA and rise rate of triplet ESA, the ISC quantum efficiency of BF_2DCz NPs was estimated to be as high as ~90.3% according to previous studies. [32] Owing to the high PL and ISC efficiencies, multiple-photon absorption, and oxygen-sensitive emission properties, BF_2DCz NPs holds tremendous potential in developing an advanced theranostic platform for biomedical applications.

Prior to investigating the imaging and therapeutic functions of BF_2DCz-BSA, their biosafety in cells was systematically evaluated. The intracellular cytotoxicity of BF_2DCz-BSA at various concentrations was studied on HeLa cells (cervical cancer cell line) and MCF-7 cells (breast cancer cell line). The cell survival rate surpassed over 90%, even at a relatively high concentration (up to 100 ppm) after culturing for 48 hours (Figure S12), implying the negligible cytotoxicity of BF_2DCz-BSA. The hemolysis experiment was then performed to analyse the biocompatibility of BF_2DCz-BSA in blood samples. Hemolysis is a process of breaking down of red blood cells, and it is critical for evaluating the safety and biocompatibility of nanoparticles in the body. [33] This experiment was evaluated for a wide range of NPs concentrations from 0 to 200 ppm. Positive and negative controls included deionized (DI) water and PBS, respectively. Hemolysis was barely observed within a pre-set concentration range (Figure S13), which demonstrates the excellent hemocompatibility of BF_2DCz-BSA, and not causing any damage to the blood cells.

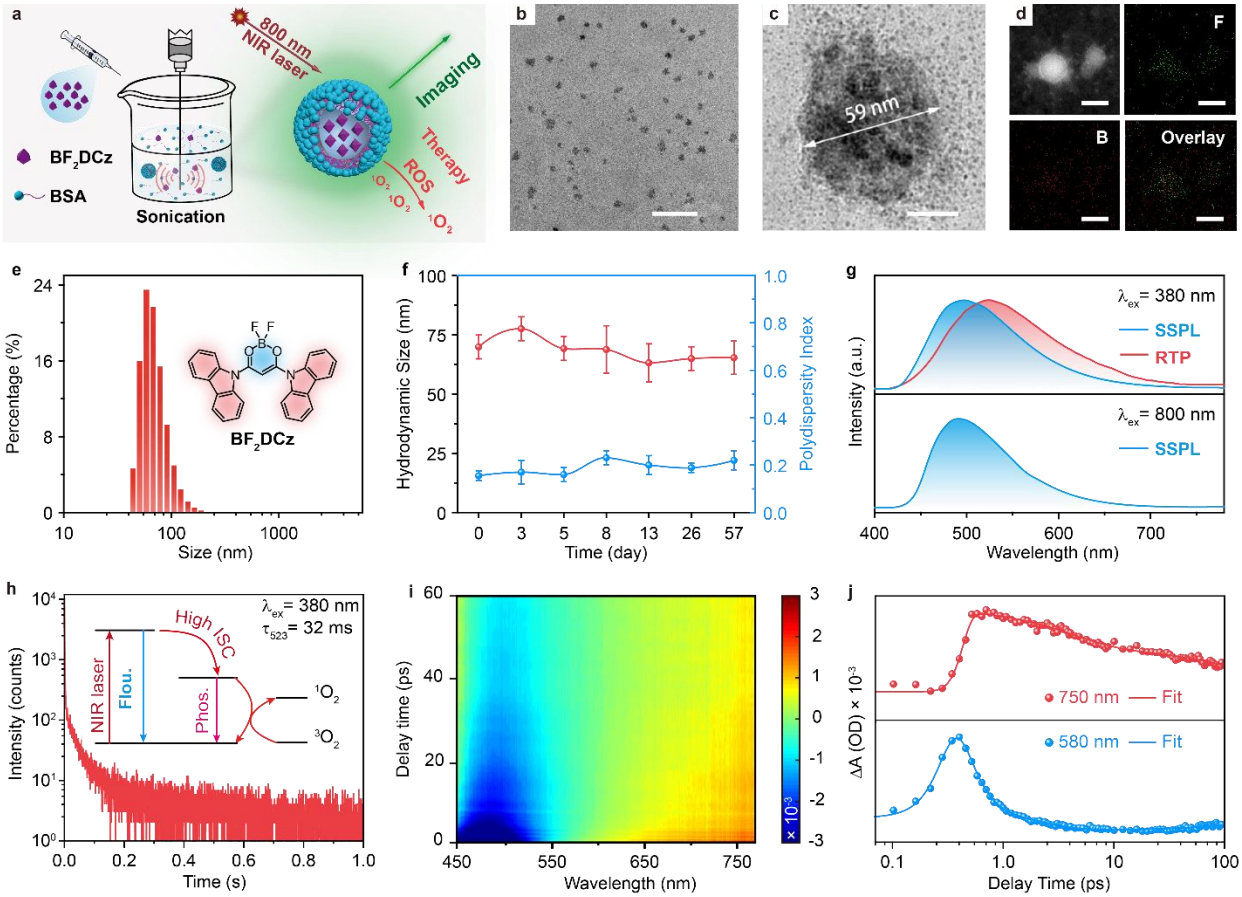

Figure 1. Fabrication and characterization of BF_2DCz-BSA. (a) Schematic illustration for the fabrication process of BF_2DCz-BSA and its imaging and therapeutic applications. (b) TEM image of BF_2DCz-BSA with low magnification (Scale bar, 500 nm). (c) HR-TEM image of a representative BF_2DCz-BSA (Scale bar, 20 nm). (d) HAADF-STEM and the corresponding EDX elemental mapping of representative BF_2DCz-BSA (Scale bar, 20 nm). (e) The hydrodynamic size of BF_2DCz-BSA in PBS buffer. Inset shows the molecular structure of BF_2DCz. (f) The colloidal stability of BF_2DCz-BSA assessed by DLS in two months (red curve indicates the hydrodynamic size, blue curve indicates the polydispersity index). (g) Steady-state photoluminescence (blue) and phosphorescence (pink) spectra excited by 380 nm UV light and 800 nm NIR laser. (h) Phosphorescence lifetime decay profile emission band at 523 nm (The insert scheme demonstrates the energy decay pathway of BF_2DCz). (i) Contour plot of fs-TA recorded. (j) Population dynamics of the singlet (blue) and triplet (pink) excited state at 580 and 750 nm, respectively.

The cellular uptake and imaging ability were firstly evaluated by confocal laser scanning microscopy (CLSM). After incubating BF_2DCz-BSA with MCF-7 cells, a large number of bright green dots can be observed in the cytoplasm with a homogeneous distribution around the nucleus (Figure S14a). When excited with the 800 nm femtosecond laser, a similar distribution of NPs in the cytoplasm was observed using multiphoton microscopy (Figure S14b). To further identify the mechanism of cellular internalization of BF_2DCz-BSA, treated MCF-7 cells were stained with LysoTracker Red, red fluorescence agent labelling lysosomes. With increasing incubation time, the green fluorescence from BF_2DCz-BSA and red fluorescence from LysoTracker Red gradually overlapped, resulting in yellow spots. However, numerous green dots were disassociated with red-labeled lysosomes when the co-incubation time was extended to 4 hours. These phenomena suggested that BF_2DCz-BSA is first internalized into lysosomes, but quickly escapes to the cytosol (Figure 2a). Furthermore, the intensity line profile in the area, indicated by the yellow arrow, shows that the bright green dots are of sub-micrometer size, similar to the size of lysosomes in MCF-7 cells (~1 μm) [34]. This phenomenon was further confirmed by another important observation that only weak fluorescence signals were obtained in MCF-7 cells when incubated with BF_2DCz-BSA in a 4℃ culturing environment for different durations of time. These results reveal that the cellular internalization is mostly inhibited, indicating that the cell uptake of BF_2DCz-BSA presents energy dependent active transport rather than passive diffusion. (Figure S15). We performed flow cytometry analysis to quantitatively analyse the cell uptake to BF_2DCz-BSA (Figure 2b). An almost linear relationship between the concentration of NPs applied and the intercellular fluorescence intensity was observed, demonstrating efficient and controllable cellular uptake of BF_2DCz-BSA (Figure S16).

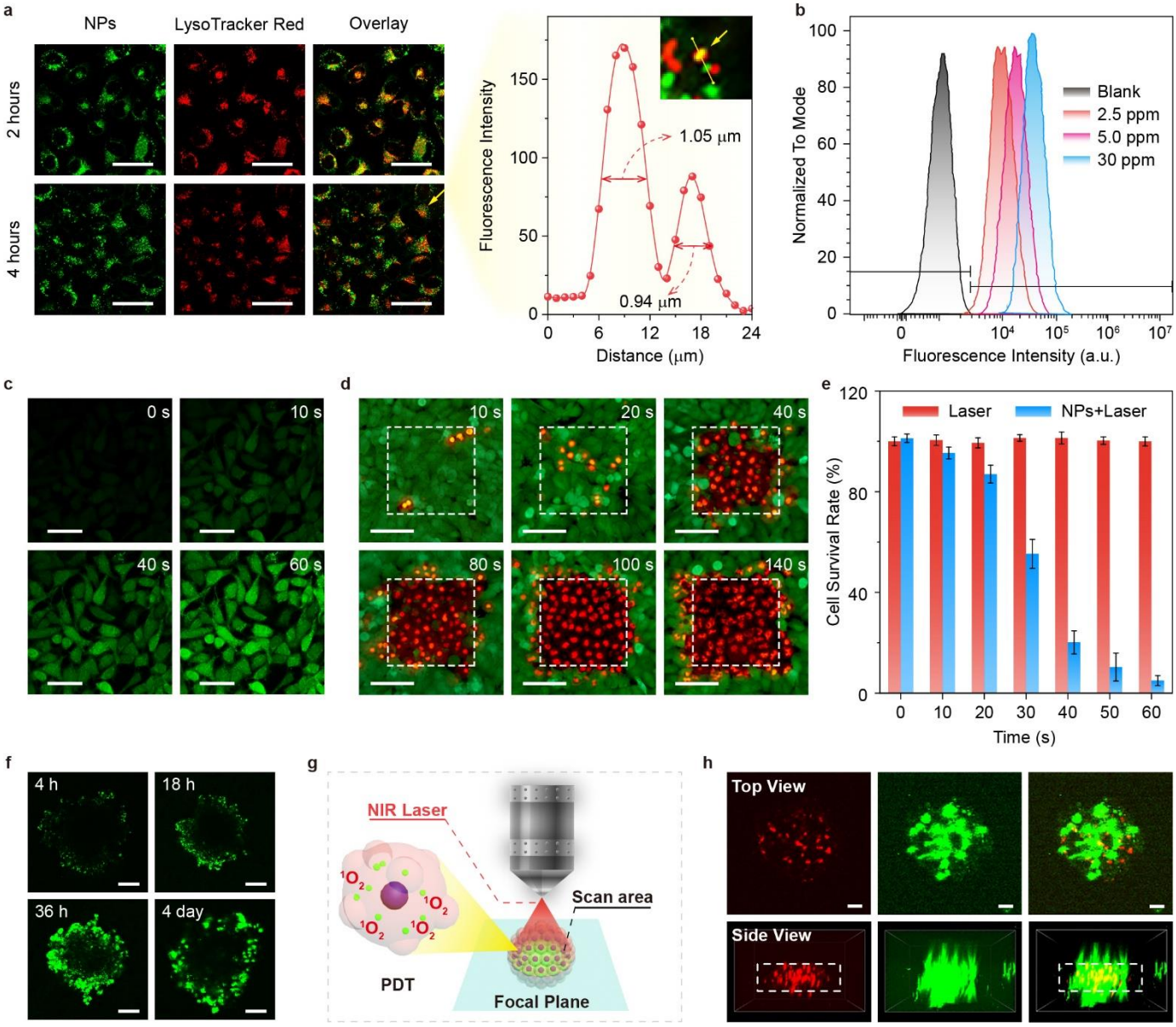

Figure 2. The cellular uptake and in vitro photodynamic properties of BF_2DCz-BSA. (a) The intracellular uptake of BF_2DCz-BSA with different incubation time at 37 ℃ (Scale bar, 25 μm). The yellow arrow and enlarged image indicate the size of BF_2DCz-BSA -encapsulated endosome and lysosome. (b) The flow cytometry result of MCF-7 cells which incubated with BF_2DCz-BSA of different concentrations. (c) The evaluation of intracellular ROS production using H_2DCFDA in MCF-7 cells incubated with BF_2DCz-BSA followed by two-photon excitation. The green fluorescence images of DCF are acquired under the excitation of 950 nm (4 mW), with the emission range of 500-550 nm (Scale bar, 50 μm). (d) The necrosis development of MCF-7 cells in response to BF_2DCz-BSA. MCF-7 cells were incubated with BF_2DCz-BSA and irradiated for different time durations. The white dashed line in all images imply the laser scanned area (200 μm × 200 μm). Scanning laser: 800 nm, 4 mW (Scale bar, 100 μm). (e) The dark and photo-toxicity of MCF-7 cells incubated with different concentrations of BF_2DCz-BSA measured by MTT assay. (f) The two-photon images of MCF-7 cell spheroids incubated with BF_2DCz-BSA for 4 hours to 4 days. Maximum intensity projections at the middle of spheroids are shown. Scanning laser: 800 nm, 4 mW (Scale bar, 50 μm). (g) The schematic illustration of TP-PDT on cell spheroid. The maximum section of spheroid is regarded as the scanned area. (h) 3D reconstructed two-photon image of MCF-7 cell spheroids after exerting TP-PDT at the scanned area. The red fluorescence of PI indicates the necrosis cell. The green fluorescence demonstrates the distribution of BF_2DCz-BSA. The PI fluorescence signals are obtained under the excitation of 1020 nm (4 mW) (Scale bar, 50 μm).

The remarkably high ISC quantum efficiency (~90.3%) of BF_2DCz-BSA lays solid foundation for PDT. Upon excitation with light, the ROS generated by photosensitizers will induce necrosis or apoptosis [35] of the target cells, due to the oxidation of a large range of biomolecules (lipids, proteins, and nucleic acids). [36] Herein, to clarify the specific type of ROS generated by BF_2DCz-BSA, four different ROS indicators, including dichlorodihydrofluorescein (DCF), singlet oxygen sensor green (SOSG), dihydrohodamine 123 (DHR123), and hydroxyphenyl fluorescein (HPF), which for the detection of overall ROS, $^1O_2$, superoxide radical, and hydroxyl radical, have been used. 405 nm laser was used to investigate the ROS production. As shown in Figure S17a, after 5 minutes of irradiation, distinct fluorescence enhancement was observed from DCF and SOSG. In addition, the phosphorescence spectrum of $^1O_2$ has also been recorded when BF_2DCz-BSA was activated (Figure S17b). According to these results, $^1O_2$ is the dominant type of ROS for PDT.

The intracellular $^1O_2$ productivity of BF_2DCz-BSA was then evaluated. MCF-7 cells were incubated with BF_2DCz-BSA and Ce6-BSA, and further excited by 405 nm light. Ce6 is a biosafe photosensitizer that has been approved for clinical application by the US Food and Drug Administration (FDA), [37] and it was herein introduced as a positive control. Afterwards, under light irradiation, cell membrane deformation was observed in the exposed areas of BF_2DCz-BSA and Ce6-BSA-treated cells (Figure S18). In contrast, MCF-7 cells treated with BF_2DCz-BSA and a 405 nm laser has no blebs on the cell membrane, supporting good compatibility of BF_2DCz-BSA (Figure S19-20). These results imply the strong photo-toxicity of BF_2DCz-BSA upon single-photon excitation. The intracellular $^1O_2$ generation was confirmed by staining with SOSG dye. As shown in Figure S21, with increasing irradiation time, the intracellular green fluorescence of SOSG increased gradually.

The ROS generation under two-photon excitation was further evaluated using the H2DCFDA dye to indicate intracellular $^1O_2$ (Detailed information is shown in the *Experimental Section*). The selected area of cells was scanned by the NIR-I laser (800 nm) for different time duration (Figure 2c). With prolonged laser exposure, the fluorescence from DCF was gradually enhanced, implying the robust intracellular $^1O_2$ conversion. In contrast, no green fluorescence was observed in Ce6-BSA treated- and PBS treated-cell samples under 800 nm laser irradiation. These results reveal excellent $^1O_2$ production of BF_2DCz-BSA in cells under two-photon excitation. To better evaluate and compare the ROS production rate of Ce6-BSA and BF_2DCz-BSA under two-photon excitation, liquid samples with DCF were loaded into glass capillary (*Experimental Section*). As shown in Figure S22, after 100 laser scans, the fluorescence intensity of DCF for BF_2DCz-BSA is about sevenfold higher than that for Ce6-BSA. The dynamic changes of MCF-7 cells were further studied under 800 nm excitation to investigate the intracellular $^1O_2$ generation. The small blebs started appearing after 40 seconds of photoexcitation, and their size and number increased continuously the prolonged exposure time (Figure S23). This phenomenon was similar to the irradiation of BF_2DCz-BSA-treated cells by a single photon laser in Figure S18. However, two-photon excitation provides more precise control on cells damage owing to optical sectioning properties [38].

The stereotactic two-photon activated PDT of BF_2DCz-BSA was further investigated on MCF-7 cells by the Calcein-AM/Propidium Iodide (PI) double staining method. After the 800 nm laser exposure on cell samples, Calcein-AM (green color) and PI (red color) dye was applied to indicate the population of survival and necrotic cells, respectively. Sequential scanning with the 800 nm laser was performed on MCF-7 cells with the exposure area of (200 μm × 200 μm). The cells outside the exposed areas mostly exhibited green fluorescence of Calcein-AM, suggesting negligible dark toxicity of BF_2DCz-BSA (Figure 2d). Within the exposed areas, the number of PI-positive cells, emitting red fluorescence, increased gradually with prolonged laser exposure time, suggesting a highly efficient two-photon activated photodynamic effect (Figure 2e). Specifically, almost all cancer cells become necrotic after 60 s of laser exposure. The highly efficient PDT effect may be attributed to the remarkably high ISC quantum efficiency of ~90.3% of BF_2DCz-BSA, which possesses a strong capability to convert triplet oxygen into singlet oxygen. In addition, no cell death occurred in MCF-7 cells (without BF_2DCz-BSA) under laser exposure, indicating negligible phototoxicity of the NIR laser with the power of 4 mW. These results showed that BF_2DCz-BSA possesses a distinct and precise therapeutic effect at the horizontal level, allowing precise cell killing in the focal plane.

To acquire further insight on two-photon activated PDT in cancer treatment, 3D tumour spheroids were prepared to investigate the cellular internalization and therapeutic effect of BF_2DCz-BSA. Tumour spheroids with diameter of ~200 μm were incubated with BF_2DCz-BSA. With longer incubation time, green fluorescence gradually spreads from the periphery to the inside of the spheroids (Figure 2f). When the spheroids were incubated with BF_2DCz-BSA for over 36 hours, a maximum penetration depth of 50 μm was achieved. This phenomenon could be understood by the passive diffusion of BF_2DCz-BSA into tumour spheroids. To study the photodynamic therapeutic effect of BF_2DCz-BSA, the treated

tumour spheroids were scanned at the depth of 100 μm with the 800 nm femtosecond laser, as illustrated in Figure 2g. PI was further applied to stain the spheroids to distinguish necrotic cells from survival ones. Interestingly, after laser exposure, red fluorescence appeared in the middle of the scanned area (Figure 2h). This can be explained by the membrane disruption of periphery cells induced by $^1O_2$ generation triggered by two-photon excitation. The released $^1O_2$ and BF_2DCz-BSA could potentially change the permeability of inner cell membrane and attack the inside cells. A "sandwich-like" distribution of fluorescence, with red emission of PI evenly distributed at the middle, indicates the precise PDT treatment at the vertical level. By analysing the fluorescence signals at five depths between 0 and 200 μm, most necrotic cells located at the depth of 100 μm were clearly visualized (Figure S24). In contrast, cells outside the scanned plane present negligible red fluorescence emission. These results suggest that BF_2DCz-BSA-triggered two-photon activated PDT enables precise tumour cell ablation at a specified depth without damage to the out-of-focus cells. The findings on the internalization of spheroid and therapeutic actions of BF_2DCz-BSA provide preliminary results for future anti-cancer applications.

The as-prepared BF_2DCz-BSA has shown good photostability and efficient *in vitro* two-photon activated PDT effects. All these features endow BF_2DCz-BSA with great potential in photo-theranostic applications. To investigate its capability for deep tissue fluorescence imaging and therapy, a mouse model with a cranial window was prepared. Briefly, a small optical window with 4 mm-diameter was made on the mouse skull to allow light access to the brain (Figure S25a). BF_2DCz-BSA suspended in PBS solution (1×) with dosage of 5 mg/kg were intravenously injected into the mouse. Under anesthesia, the mouse was immobilized on a home-made stereotactic setup (Figure S25b), and the body temperature was maintained by a heating pad. A femtosecond laser at a wavelength of 800 nm was applied on the mouse brain to conduct two-photon imaging (Figure 3a). As shown in Figure 3b, the 3D reconstructed fluorescent images clearly reveal the brain vasculature network with low background noise. Both big blood vessels and small blood capillaries are easily distinguishable by fluorescent images at various depths. The sectioning images of brain vasculature at specific depths are shown in Figure 3c,d. The strong brightness of fluorescence emission resulted from the high quantum yield and good colloidal stability of BF_2DCz-BSA. The contrasting capability of the two-photon imaging was further evaluated by the signal-to-background ratios (SBR) of the obtained fluorescent images (Figure S26). Line profiles of the fluorescence intensity on selected blood vessels at specific depth were assessed, and the SBR was calculated based on the fluorescence intensity between blood vessels and the background. The SBR value on the selected brain blood vessel was calculated to be 234 at 30 μm, which gradually decayed to 8 at the imaging depth of 500 μm. This phenomenon is attributed to the attenuation of the incident light as the penetration depth increased. In addition, the blood flow speed can also be measured by two-photon imaging. The standard line scan technique was applied on the selected blood vessel. As shown in Figure S27, the line scan images are acquired along the yellow lines in each 2D image at 4.8 μs per pixel, and the vertical direction denotes the scan speed at 3.665 ms per pixel. The line scan images show tilted stripes, indicating the flowing of unlabelled blood cells. The blood flow speed can be measured by calculating the slope of the stripes. The measured results were 1.05 ± 0.03, 0.77 ± 0.03, and 0.80 ± 0.02 mm/s for selected blood vessels at depths of 200, 400, and 530 μm.

The *in vivo* deep-tissue PDT was demonstrated by selective blood vessel closure. Selective closure of blood vessel is a promising technique for neoplastic diseases [39], which require high spatial control to conduct treatment on complex organs. In our study, a cerebral micro-vessel with a diameter of 5 μm at the depth of 100 μm was precisely closed under the navigation of fluorescence imaging from BF_2DCz. By continuously irradiating the target for 3 minutes, the fluorescence on the scanned area and the following vein was significantly quenched, which verified the occurrence of vessel closure (Figure S28). However, by further deepening the imaging depth to 200 μm, the action of blood vessel closure was largely restricted, which is attributed to the attenuated laser power in deep tissue. Generally, the results indicate that BF_2DCz-BSA with good biocompatibility, negligible biotoxicity, high fluorescence brightness, and efficient PDT effect hold great promise for image-guided photo-theranostic applications.

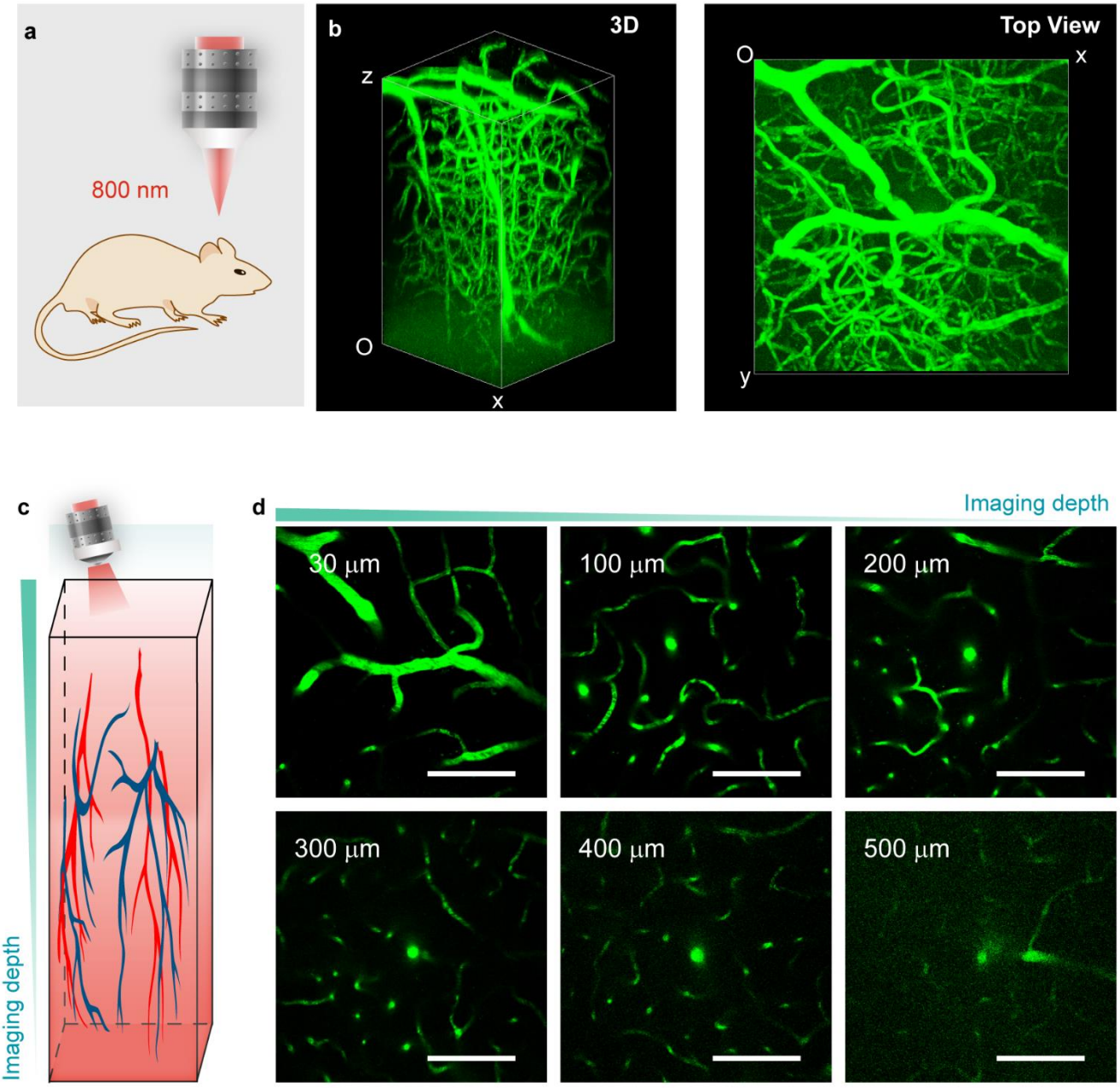

Figure 3. *In vivo* two-photon imaging on brain vasculature of mouse. (a) The schematic illustration of brain vascular imaging. (b) The 3D reconstruction and top view of brain vasculature (The imaging area is set as 318.2 μm × 318.2 μm and the deepest imaging depth is 568 μm). (c) The schematic illustration of vasculature imaging. (d) The fluorescent imaging of cortical vasculature at various penetration. (Scale bar, 100 μm).

Considering the importance of biosafety in biomedical applications and future clinical translation, the potential systemic toxicity of BF_2DCz-BSA was carefully assessed. The *in vivo* distribution of BF_2DCz-BSA was first investigated by *in vivo* fluorescence imaging after intravenous injection. As shown in Figure S29, BF_2DCz-BSA mainly accumulated in the liver and kidneys. With increasing feeding time, the fluorescence in liver was largely enhanced while that of the kidneys reduced slightly. This phenomenon implies that both liver and urine are major routes that metabolize BF_2DCz-BSA. Different dosages (5, 10, and 20 mg/kg) of BF_2DCz-BSA were intravenously injected into three groups of BALB/C mice, and PBS treated mice were introduced as the control group. The body weight of the treated mice showed no evident fluctuations, indicating minimal systemic effects (Figure S30). The size of BF_2DCz-BSA is similar to viruses and large antigens, [40]and therefore their immunogenicity may activate the immune system and induce an acute inflammatory response, which is reflected by monitoring the changes of hematological factors (such as red and white blood cell count). Accordingly, a complete blood routine test was conducted to investigate the immune response to

BF_2DCz-BSA (Figure 4(a-f) and Figure S31). Results showed no distinct variation in the 14 hematological indicators compared with the control and reference values, indicating no acute toxicity of BF_2DCz-BSA. Similarly, serum biochemistry assays (Figure 4(g-l) and Figure S32) indicated that four indicators of liver function (ALT, ALB, AST, and TP) and four indicators of kidney function (UREA, CREA, UA, and GLB), three indicators of blood lipid (HDL-C, LDL-C, and TG), and one indicator of blood glucose (GLU) were normal, suggesting minimal interference of BF_2DCz-BSA in the metabolic activities of major organs. After 15 days of intravenous administration, histological analysis was performed on the tissue sections obtained from four groups of treated mice. All pathological sections (heart, liver, spleen, lung, kidney, and brain) were carefully assessed by a pathologist (Figure 4m, Figure S33-34). Lymphocyte infiltration was absent in all organs. There was no abnormal cell morphology identified in the myocardial fibers and brain. Accordingly, no fibrosis was detected in the lung and liver tissue sections. Normal white and red pulp structures were clearly observed in the spleen tissue sections. No abnormal glomerulus and tubules structures were detected in the kidney sections. Tissue necrosis was absent from all histological samples. These results offer preliminary evidence that BF_2DCz-BSA, even at a high dosage of 20 mg/kg, cannot cause acute toxicity in BALB/c mice during the assessment period, indicating the potential of BF_2DCz-BSA to be translated for clinical applications.

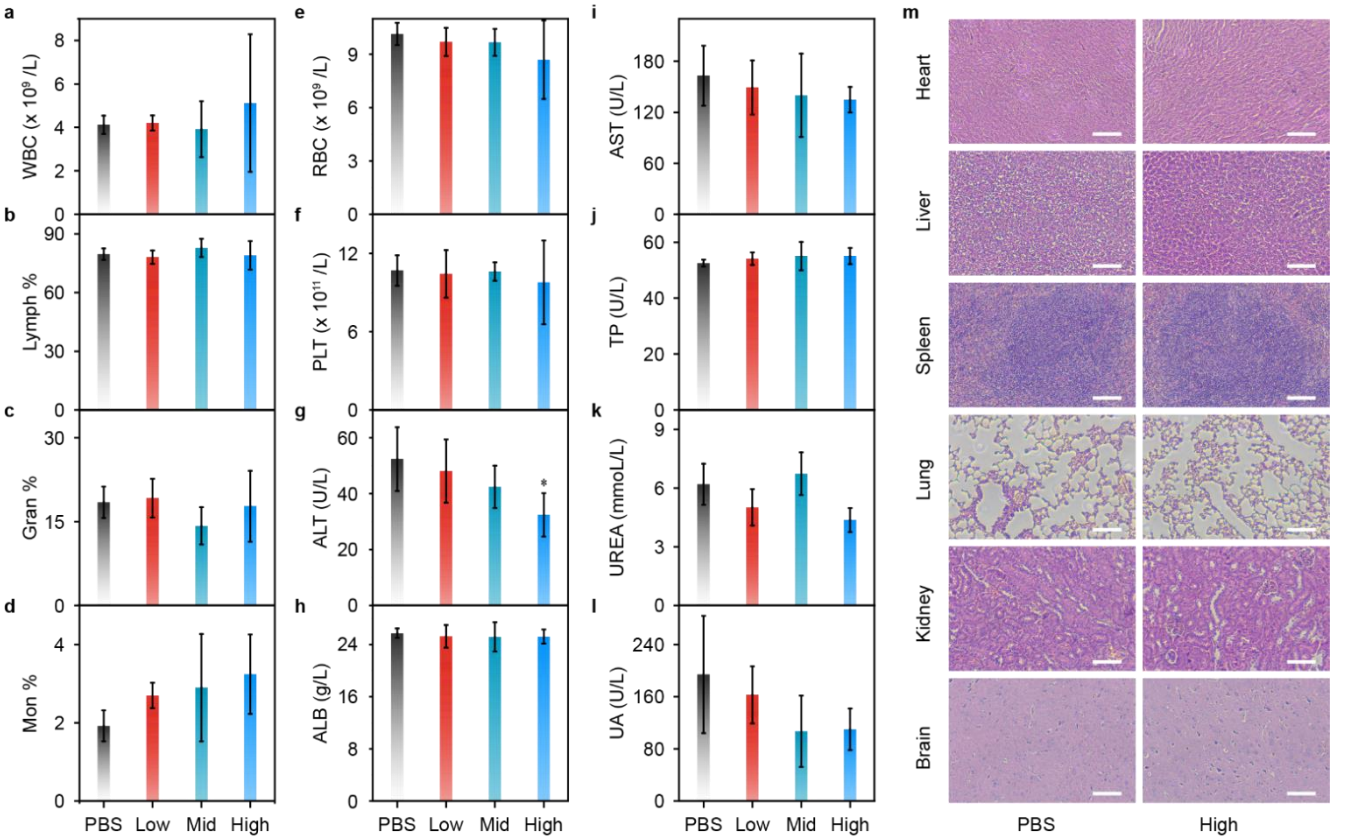

Figure 4. *In vivo* biocompatibility assessment of BF_2DCz-BSA (a-l) Blood test results for treated BALB/c mice. The results show no abnormalities in immune response, kidney and liver functions, blood chemistry by applying four dose schemes PBS and BF_2DCz-BSA-treated groups (Low Conc.=5 mg/kg, Mid Conc.=10 mg/kg, High Conc.=20 mg/kg) (n=5). Abbreviations: white blood cell count, WBC; lymphocyte cell percentage, Lymph%; monocyte cell percentage, Mon%; granulocyte cell percentage, Gran%; red blood cell count, RBC; platelet count, PLT; alanine transaminase, ALT; albumin, ALB; aspartate transaminase, AST; total protein, TP; blood urea nitrogen, UREA; Uric acid, UA. (m) Histological images of the major organs (heart, liver, spleen, lung, kidney, and brain) of mice at the end of 15 days after intravenous injection of PBS buffer and BF_2DCz-BSA suspension with dosage of 20 mg/kg (Scale bar,100 μm).

Conclusions

A metal-free organic material (BF_2DCz) with RTP characteristics was successfully fabricated. The prepared BF_2DCz exhibit a high PLQY of 47.7 ± 3% and impressive intersystem crossing (ISC) efficiency of ~90.3%. Using BSA as the capping agent, BF_2DCz-BSA exhibits monodispersity, superior photostability, negligible dark toxicity, and excellent biocompatibility in the physiological environment. Upon excitation with a NIR femtosecond laser, a precise PDT was achieved at both horizontal and vertical levels in cell samples, indicating its high spatial-temporal controls and promising anti-cancer effects. Furthermore, two-photon imaging on the mouse brain vasculature and selective blood vessel closure were realized using BF_2DCz-BSA as a therapeutic agent. This study provides a novel strategy to advance the clinical application of photosensitizers for highly efficient deep-tissue photodynamic therapy.

Author Contributions

Zhourui Xu: Conceptualization, Investigation, Methodology, Writing-original draft. **Yihang Jiang:** Investigation, Methodology. **Yuanyuan Shen, Lele Tang, Zulu Hu:** Methodology. **Guimiao Lin, Wing-cheung Law, Mingze Ma, Biqin Dong:** Resources. **Kentye Yong, Gaixia Xu:** Supervision. **Ye Tao, Runfeng Chen, Chengbin Yang:** Conceptualization, Project administration, Validation, Visualization, Writing-review&editing.

Conflicts of interest

There are no conflicts to declare.

Acknowledgements

This work was financially supported by National Natural Science Foundation of China (81801859, 31871442, 12074269, 22075149 and 61875090), Natural Science Foundation of Guangdong Province (2019A1515012163, 2021A1515012159), Guangdong Medical Science and Technology Research Funding(A2019359), University Stable Support Research Funding of Shenzhen (20200813153346001), the Research Grants Council of the Hong Kong Special Administrative Region, China (PolyU 15208720), Basic Research Foundation of Shenzhen (JCYJ20180305125254860), the "Jiangsu Specially-Appointed Professor Plan", the Six Talent Plan of Jiangsu Province (XCL-049), and a Start-up Grant from Shenzhen University (2019136). The authors greatly appreciate the help from the Instrumental Analysis Center of Shenzhen University for the assistance with imaging analysis. Animal experiment is in accordance with the regulations of the Animal Ethical and Welfare Committee of Shenzhen University (AEWC-SZU).

References

1. X. Li, J. F. Lovell, J. Yoon and X. Chen, *Nat. Rev. Clin. Oncol.*, 2020, **17**, 657-674.
2. R. Baskaran, J. Lee and S. G. Yang, *Biomater. Res.*, 2018, **22**, 25.
3. S. S. Lucky, K. C. Soo and Y. Zhang, *Chem. Rev.*, 2015, **115**, 1990-2042.
4. F. Hu, S. Xu and B. Liu, *Adv. Mater.*, 2018, **30**, 1801350.
5. B. Yang, Y. Chen and J. Shi, *Chem. Rev.*, 2019, **119**, 4881-4985.
6. X. Wen, Y. Li and M. R. Hamblin, *Photodiagnosis Photodyn. Ther.*, 2017, **19**, 140-152.
7. R. L. Yanovsky, D. W. Bartenstein, G. S. Rogers, S. J. Isakoff and S. T. Chen, *Photodermatol. Photoimmunol. Photomed.*, 2019, **35**, 295-303.
8. C. M. Moore, D. Pendse and M. Emberton, *Nat. Clin. Pract. Urology*, 2009, **6**, 18-30.
9. J.-J. Hu, Q. Lei and X.-Z. Zhang, *Prog. Mater Sci.*, 2020, **114**, 100685.
10. H. Huang, S. Banerjee and P. J. Sadler, *Chembiochem*, 2018, **19**, 1574-1589.
11. J. Tian, B. Huang, M. H. Nawaz and W. Zhang, *Coord. Chem. Rev.*, 2020, **420**, 213410.
12. K.-N. Wang, L.-Y. Liu, G. Qi, X.-J. Chao, W. Ma, Z. Yu, Q. Pan, Z.-W. Mao and B. Liu, *Adv. Sci.*, **n/a**, 2004379.
13. J. S. Nam, M.-G. Kang, J. Kang, S.-Y. Park, S. J. C. Lee, H.-T. Kim, J. K. Seo, O.-H. Kwon, M. H. Lim, H.-W. Rhee and T.-H. Kwon, *J. Am. Chem. Soc.*, 2016, **138**, 10968-10977.
14. L. Zhang, Y. Li, W. Che, D. Zhu, G. Li, Z. Xie, N. Song, S. Liu, B. Z. Tang, X. Liu, Z. Su and M. R. Bryce, *Adv. Sci. (Weinh)*, 2019, **6**, 1802050.
15. K. Li, Y. Chen, J. Wang and C. Yang, *Coord. Chem. Rev.*, 2021, **433**, 213755.
16. M. Kang, C. Zhou, S. Wu, B. Yu, Z. Zhang, N. Song, M. M. S. Lee, W. Xu, F.-J. Xu, D. Wang, L. Wang and B. Z. Tang, *J. Am. Chem. Soc.*, 2019, **141**, 16781-16789.
17. Y. Liu, X. Meng and W. Bu, *Coord. Chem. Rev.*, 2019, **379**, 82-98.
18. B. Gu, W. Wu, G. Xu, G. Feng, F. Yin, P. H. J. Chong, J. Qu, K.-T. Yong and B. Liu, *Adv. Mater.*, 2017, **29**, 1701076.
19. S. Fischer, R. D. Mehlenbacher, A. Lay, C. Siefe, A. P. Alivisatos and J. A. Dionne, *Nano Lett.*, 2019, **19**, 3878-3885.
20. W. Zhao, Z. He and B. Z. Tang, *Nat. Rev. Mater.*, 2020, **5**, 869-885.
21. S. Hirata, *Advanced Optical Materials*, 2017, **5**, 1700116.
22. E. Oh, R. Liu, A. Nel, K. B. Gemill, M. Bilal, Y. Cohen and I. L. Medintz, *Nat. Nanotechnol.*, 2016, **11**, 479-486.
23. H. Ma, Q. Peng, Z. An, W. Huang and Z. Shuai, *J. Am. Chem. Soc.*, 2019, **141**, 1010-1015.
24. X. Zhen, Y. Tao, Z. An, P. Chen, C. Xu, R. Chen, W. Huang and K. Pu, *Adv. Mater.*, 2017, **29**, 1606665.

25. J. Jin, H. Jiang, Q. Yang, L. Tang, Y. Tao, Y. Li, R. Chen, C. Zheng, Q. Fan, K. Y. Zhang, Q. Zhao and W. Huang, *Nat. Commun.*, 2020, **11**, 842.
26. Y. Su, S. Z. F. Phua, Y. Li, X. Zhou, D. Jana, G. Liu, W. Q. Lim, W. K. Ong, C. Yang and Y. Zhao, *Sci. Adv.*, 2018, **4**, eaas9732.
27. J. Wang, Z. Huang, X. Ma and H. Tian, *Angew. Chem. Int. Ed.*, 2020, **59**, 9928-9933.
28. Q. Dang, Y. Jiang, J. Wang, J. Wang, Q. Zhang, M. Zhang, S. Luo, Y. Xie, K. Pu, Q. Li and Z. Li, *Adv. Mater.*, 2020, **32**, 2006752.
29. Y. Shen, A. J. Shuhendler, D. Ye, J.-J. Xu and H.-Y. Chen, *Chem. Soc. Rev.*, 2016, **45**, 6725-6741.
30. L. Wu, J. Liu, P. Li, B. Tang and T. D. James, *Chem. Soc. Rev.*, 2021, **50**, 702-734.
31. G. Feng and B. Liu, *Acc. Chem. Res.*, 2018, **51**, 1404-1414.
32. M. Etinski, J. Tatchen and C. M. Marian, *J. Chem. Phys.*, 2011, **134**, 154105.
33. M. Manaargadoo-Catin, A. Ali-Cherif, J.-L. Pougnas and C. Perrin, *Adv. Colloid Interface Sci.*, 2016, **228**, 1-16.
34. H. Xu and D. Ren, *Annu. Rev. Physiol.*, 2015, **77**, 57-80.
35. D. Kessel and N. L. Oleinick, *Photochem. Photobiology*, 2018, **94**, 213-218.
36. M. S. Baptista, J. Cadet, P. Di Mascio, A. A. Ghogare, A. Greer, M. R. Hamblin, C. Lorente, S. C. Nunez, M. S. Ribeiro, A. H. Thomas, M. Vignoni and T. M. Yoshimura, *Photochem. Photobiol.*, 2017, **93**, 912-919.
37. S. Nasr, M. Rady, A. Sebak, I. Gomaa, W. Fayad, M. E. Gaafary, M. Abdel-Kader, T. Syrovets and T. Simmet, *Pharmaceutics*, 2020, **12**, 494.
38. S. Wang, H. Chen, J. Liu, C. Chen and B. Liu, *Adv. Funct. Mater.*, 2020, **30**, 2002546.
39. Y. Huang, Z. Wu, H. Lui, J. Zhao, S. Xie and H. Zeng, *Sci. Adv.*, 2019, **5**, eaan9388.
40. Y. M. Bar-On, A. Flamholz, R. Phillips and R. Milo, *Elife*, 2020, **9**, e57309.